

Laboratory micro-seismic signature of shear faulting and fault slip in shale

J. Sarout^a, Y. Le Gonidec^b, A. Ougier-Simonin^c, A. Schubnel^d,
Y. Guéguen^d, and D.N. Dewhurst^a

^a*CSIRO Energy, Perth, Australia*

^b*Géosciences Rennes - CNRS/INSU UMR6118, Rennes, France*

^c*British Geological Survey, Engineering Geology, Keyworth, UK*

^d*Ecole Normale Supérieure, CNRS-UMR 8538, Laboratoire de Géologie, Paris, France*

Abstract

This article reports the results of a triaxial deformation experiment conducted on a transversely isotropic shale specimen. This specimen was instrumented with ultrasonic transducers to monitor the evolution of the micro-seismic activity induced by shear faulting (triaxial failure) and subsequent fault slip at two different rates. The strain data demonstrate the anisotropy of the mechanical (quasi-static) compliance of the shale; the P-wave velocity data demonstrate the anisotropy of the elastic (dynamic) compliance of the shale. The spatio-temporal evolution of the micro-seismic activity suggests the development of two distinct but overlapping shear faults, a feature similar to relay ramps observed in large-scale structural geology. The shear faulting of the shale specimen appears quasi-aseismic, at least in the 0.5 MHz range of sensitivity of the ultrasonic transducers used in the experiment. Concomitantly, the rate of micro-seismic activity is strongly correlated with the imposed slip rate and the evolution of the axial stress. The moment

Email address: joel.sarout@csiro.au (J. Sarout)

tensor inversion of the focal mechanism of the high quality micro-seismic events recorded suggests a transition from non-shear dominated to shear-dominated micro-seismic activity when the rock evolves from initial failure to larger and faster slip along the fault. The frictional behaviour of the shear faults highlights the possible interactions between small asperities and slow slip of a velocity-strengthening fault, which could be considered as a realistic experimental analogue of natural observations of non-volcanic tremors and (very) low-frequency earthquakes triggered by slow slip events.

Keywords: Shale, P-wave velocity, Anisotropy, Micro-seismicity, Focal mechanism, Shear faulting, Fault slip, Friction

1. Introduction

Changes in the stress state can induce brittle damage (micro-fracturing) in rocks that can radiate mechanical energy in the form of Micro-Seismic (MS) activity, also called acoustic emissions [28, 31, 32]. Accumulation of damage can ultimately lead to mechanical failure of the rock. Among the various rock failure mechanisms listed in the literature, we focus here on brittle faulting pertaining to numerous geological settings observable during the deformation of rocks originating from the Earth's upper crust.

It is generally accepted that for a given material, MS activity is prominently observed during deformation under the following conditions: (i) relatively low normal stresses; (ii) relatively high shear stresses; and/or (iii) relatively high stress loading rates, e.g., [1, 51]. In the past, most research efforts published in the literature involving micro-seismic monitoring of deformation processes in the laboratory have focused either on:

- crystalline rocks in relation to earthquake/fault mechanics, geotechnical or geothermal applications, e.g., [6, 26, 29, 33]; or
- conventional reservoir rocks in relation to oil and gas exploration, production and monitoring (reservoir integrity, compartmentalisation, injection-induced fracture/fault reactivation...), e.g., in sandstones [7, 8, 9, 15, 17, 45]; or to a lesser extent in porous carbonate rocks [16].

At the field scale, several studies on the monitoring of MS activity in granites and carbonates have been published. These include the monitoring of: thermally-induced MS activity potentially associated with radioactive waste disposal in boreholes drilled in a tunnel's floor at Äspö's Hard Rock Laboratory in Sweden [37], in the Excavation Damage Zone (EDZ) in the Un-

26 derground Research Laboratory in a granitic rock mass in Canada [53, 54]
27 and injection-induced MS activity in a limestone formation in the Laboratoire
28 Souterrain à Bas Bruit in France [18]. Fewer field-scale studies on the MS
29 activity induced by faulting or fault slip in shale formations have been pub-
30 lished. A recent study demonstrated the feasibility of monitoring the time
31 evolution of MS activity associated with the EDZ in the Opalinus Clay for-
32 mation at the Mont-Terri Underground Research Laboratory in Switzerland
33 [27]. The MS activity associated with fluid injection in the Colorado Shale
34 formation was successfully monitored by [46]. In contrast, the monitoring of
35 the spatial extent of anthropogenic hydraulic fractures in stimulated oil/gas
36 reservoirs have been an active field of research since the 1980's, strongly sup-
37 ported by industry funding, especially in the recent years with the advent
38 and development of commercially-viable unconventional reservoirs such as
39 gas shales, e.g., [49].

40 At the laboratory scale, experiments have been reported on shales uni-
41 axially deformed at room conditions under large loading rates (see [2] and
42 references therein). However, no determination of spatial locations or focal
43 mechanisms of the recorded MS events (MSEs) was carried out. In addition,
44 the assessment of the frictional behaviour of the generated fractures (post-
45 failure behaviour) and the characterisation of its MS response to slip is not
46 practically feasible under such experimental conditions due to the unstable
47 nature of the induced brittle failure. MS activity and location in shale sam-
48 ples containing quartz veins have been reported by [30]. In this particular
49 case, and as expected, the MS activity seemed to coincide with the location
50 of quartz veins favorably oriented with respect to the maximum principal

51 compressive stress.

52 To our knowledge, no data on spatio-temporal localisation and focal
53 mechanism estimation of MS activity have been reported on deforming clay-
54 rich rocks such as conventional reservoir-sealing shales. Under triaxial defor-
55 mation at realistic subsurface stress conditions, the shale specimens fail in
56 shear, leading to the formation of a shear fracture. The first questions that
57 arise then for these rocks are the following: (i) can we expect precursory
58 micro-seismic activity prior to the macroscopic faulting? (ii) Would the slip
59 on the newly generated fault induce any micro-seismic activity? (iii) How
60 would the signature of the MS activity be affected by the deformation rate?

61 Due to their fine-grained nature, it is generally thought that clays act as a
62 lubricant in frictional geological environments, e.g., [36]. Also, the brittleness
63 of clay behaviour is known to be controlled by their degree of hydration (the
64 more hydrated, the less brittle), their mineral composition, and the imposed
65 deformation rate (higher rates induce a more brittle response). The lack
66 of published experimental studies on the MS activity of shales subjected to
67 stress conditions typical of the upper crust can probably be explained by the
68 inherent complexity of shales and the associated difficulty in conducting lab-
69 oratory deformation experiments on them under well-controlled conditions.
70 In addition, there is considerable technical complexity in conducting and pro-
71 cessing laboratory experiments aimed at monitoring and locating with high
72 accuracy the MS activity induced by deforming relatively small specimens.
73 In this regard, the difficulty in locating the MS activity is exacerbated by
74 the directional dependency (anisotropy) of wave propagation in shales, e.g.,
75 [11, 13, 24, 39, 40, 48].

76 In this paper, the results and analysis of a laboratory deformation experi-
77 ment in a shale specimen are reported. The specimen was triaxially deformed
78 to beyond the failure point under realistic subsurface stress conditions while
79 associated MS activity was recorded. The aim was to analyse the contrast
80 in the MS signature of shear faulting and subsequent fault slip as well as
81 the effect of the deformation rate on the fault's micro-seismic and frictional
82 response.

83 In the following pages, the experimental conditions are detailed (section
84 2) along with the main results in terms of stress-strain data, ultrasonic P-
85 wave velocity data, and micro-seismic activity (section 3). The fourth section
86 is dedicated to an analysis and discussion of these results in terms of the MS
87 signatures of shear faulting and fault slip (slow/fast slip), frictional behaviour
88 of the shear fault in relation to the associated MS activity, and a comparison
89 to other rock lithologies.

90 **2. Description of the experiment**

91 *2.1. Shale material*

92 A large core was recovered from the North Sea at a depth of 1643 m be-
93 low sea bed in a clay-rich shale formation (Campanian, upper Cretaceous).
94 The core was preserved since recovery from depth in several layers of plastic
95 and aluminium wrap with an additional external wax coating. After un-pack-
96 ing, this shale appeared relatively homogeneous, dark grey in colour, with
97 bedding visible inclined at 45° to the core axis. Twin cylindrical specimens
98 40 mm in diameter have been cored along the axis of the original core so
99 that the bedding was also inclined at 45° to their axis. Their end faces were

100 trimmed and ground to be parallel to each other to within 0.02 mm. The
101 final length of the specimens was 81 mm (long specimen) and 40 mm (short
102 specimen), respectively. For the coring, trimming and grinding operations,
103 compressed air was used as the cooling fluid. After preparation, the spec-
104 imens were equilibrated for several days at room conditions (20°C, relative
105 humidity of 50%) until stabilisation of their mass at these conditions. After
106 this initial treatment the specimens turned to a light grey colour. The mass
107 evolution of the samples during this initial treatment and their change in
108 color suggest that they lost water (dehydration) by exchange with the atmo-
109 sphere. The porosity of the shale was estimated to be of the order of 19%
110 (density: 2370 kg/m³) based on mass measurements conducted on a separate
111 block cut from the original core in its preserved state (immediately after un-
112 packing the core) and its state after mass stabilisation at a room conditions
113 (20°C, relative humidity of 50%). Note that this porosity is only a lower
114 bound estimate of the actual porosity of the shale assuming that the core
115 was fully water-saturated in its preserved state and is fully dry in its final
116 equilibrated state (20°C and relative humidity of 50%). It is expected that
117 only the so-called "free" water could have evaporated during this treatment,
118 so that the shale specimens are likely in a partially saturated state.

119 The shorter specimen was used to conduct permeability measurements
120 with nitrogen gas under increasing effective pressure using a steady state
121 method, i.e., constant gas flow imposed at one end of the specimen, and
122 monitoring of the differential pressure build-up and stabilisation across its
123 two ends [25]. The permeability results are summarised in TABLE 1. The
124 permeability of this shale to nitrogen decreases by almost two orders of mag-

125 nitude from 2.1×10^{-5} mD down to 6.9×10^{-7} mD when the effective confining
126 pressure increases from 4 MPa up to 65 MPa. This seems to indicate that
127 stress-sensitive pre-existing micro-cracks (damage) are closed by the increas-
128 ing effective pressure. Such micro-cracks might have been induced by stress
129 release following the recovery of the shale core from depth and/or the dehy-
130 dration of the specimen at room conditions during initial treatment.

131 The longer specimen was used to conduct the triaxial deformation exper-
132 iment with MS monitoring detailed in the remainder of this article.

133 *2.2. Experimental equipment*

134 In order to characterise the MS response of the shale to changes in the tri-
135 axial stress state, a specific laboratory setup is required to monitor both the
136 deformation of the specimen and the induced MS activity. The experimental
137 setup consists mainly of: (i) a *Sanchez Technologies* axisymmetric triaxial
138 stress vessel in which a radial and an axial stress can be independently applied
139 to a cylindrical rock specimen; (ii) an *Applied Seismology Consultants* multi-
140 channel ultrasonic/micro-seismic monitoring system (Fig. 1). This apparatus
141 allows the simultaneous acquisition of various types of data on a single rock
142 specimen: (i) radial and (ii) axial deformations, (iii) active ultrasonic moni-
143 toring, i.e., ultrasonic P-wave velocities along numerous propagation paths at
144 selected stages of the deformation (called velocity surveys); and (iv) passive
145 monitoring, i.e., induced micro-seismicity (also called acoustic emissions).
146 Note that both active and passive monitoring are conducted using the same
147 array of ultrasonic transducers as described below.

148 After the initial drying treatment of the long shale specimen at a temper-
149 ature of 20°C and a relative humidity of 50%, four strain gauges are glued

150 onto its lateral surface so that four independent directions of deformation
151 are measured (see Figs. 1 and 2): Gauge 1 measures the axial strain along
152 the specimen's axis, at 45° to the bedding orientation. Gauge 2 measures
153 the circumferential strain orthogonal to the specimen's axis, at 45° to the
154 bedding; this strain also corresponds to the radial strain, and for sake of
155 simplicity, it will be referred to as radial strain in the remaining of the ar-
156 ticle. Gauge 3 measures the strain orthogonal to the bedding, at 45° to the
157 specimen's axis. Gauge 4 measures the strain along the bedding, at 45° to
158 the specimen's axis. In addition, the average axial displacement between the
159 two ends of the specimen was monitored using three contactless Eddy current
160 displacement transducers located outside the pressure vessel.

161 2.3. *Experimental protocol*

162 The shale specimen is inserted into a flexible *Viton* sleeve and placed
163 inside the pressure chamber of the triaxial stress vessel, which is then closed
164 and filled with oil. The purpose of the flexible sleeve is to isolate the specimen
165 from the hydraulic oil used to apply the radial stress [40]. This specimen is
166 instrumented with: (i) four strain gauges glued directly to its lateral surface,
167 at mid-height; (ii) an array of 16 miniature ultrasonic transducers (6 mm in
168 diameter) made of piezo-ceramic material with a central resonant frequency
169 of about 0.5 MHz. These transducers can be used as ultrasonic sources or
170 receivers attached directly to the lateral surface of the specimen, through
171 sealable holes in the flexible *Viton* sleeve (Fig. 2).

172 The experimental deformation protocol consists of: (i) an isotropic stress
173 loading to subject the specimen to a simulated *in situ* condition with a
174 confining pressure of 10 MPa; (ii) a deviatoric stress loading at a constant

175 axial displacement rate of 1 mm/h ($3.5 \times 10^{-6} \text{ s}^{-1}$) up to a point beyond the
176 specimen's failure, which is indicated by a peak in the recorded deviatoric
177 stress; then (iii) a sudden increase of the displacement rate to 10 mm/h
178 ($3.5 \times 10^{-5} \text{ s}^{-1}$) until stabilisation of the recorded deviatoric stress (Fig. 3).
179 The deformation experiment is conducted without injecting water and with-
180 out controlling the pore pressure at the two ends of the specimen. In view of
181 the testing conditions (partial saturation, no pore fluid injection, and no pore
182 pressure control), the deformation of the specimen is considered as macro-
183 scopically drained. Furthermore, the water saturation state and type (uni-
184 form or patchy) of the specimen being unknown, the water diffusion length
185 scale within the specimen is also unknown. Therefore, whether the defor-
186 mation is locally (in the vicinity of the pore water) drained or undrained is
187 unknown.

188 The aim of the deviatoric stress loading is two-fold: (i) assess the effect
189 of shear faulting and fault slip on the MS response of a shale; and (ii) as-
190 sess the effect of fault slip rate on the MS activity. The active and passive
191 monitoring equipment is controlled with the *Xtream* software, while the data
192 management and processing is conducted with the *Insite Seismic Processor*
193 software.

194 As part of the active ultrasonic monitoring, at selected stages of the
195 experiment, a P-wave velocity survey is conducted. Each survey consists
196 of 16 consecutive shots, one from each transducer acting as a source. For
197 each source transducer shot, the transmitted waveforms are recorded on the
198 15 remaining transducers which act as receivers. The waveform recorded at
199 each receiver corresponds to the mechanical vibration transmitted through

200 the rock specimen from the source transducer to that particular receiver. In
201 order to improve the signal-to-noise ratio (SNR), each waveform is in fact the
202 result of the stack of several tens of shots from a given source transducer. The
203 waveforms are recorded with a sampling rate of 10 MHz and an amplitude
204 resolution of 12 bits. Each source-receiver pair defines a particular ray path
205 within the specimen, i.e. different directions of wave propagation relative to
206 the specimen's axis and therefore relative to the shale bedding. Each velocity
207 survey typically lasts 30 seconds and consists of 240 waveforms (recorded over
208 82 microseconds), half of which corresponds to different ray paths within the
209 volume of the specimen. The ultrasonic survey data set acquired during the
210 experiment consists of 10 surveys recorded during the isotropic stress loading
211 after every one or two MPa of confining pressure, and 11 surveys recorded
212 during the deviatoric stress loading.

213 Between two consecutive velocity surveys, the ultrasonic/micro-seismic
214 system is switched to the passive monitoring mode in order to record any
215 MS activity induced by the stress loading. In this mode, the voltages gen-
216 erated by the ultrasonic transducers sensing a given Micro-seismic events
217 (MSE) are recorded according to a pre-defined trigger logic. Typically, if five
218 transducers exceed a voltage threshold of 15 mV within a time window of
219 500 nanoseconds, the waveforms from all 16 transducers are recorded for a
220 time window of 82 microseconds. These waveforms are also recorded with a
221 sampling rate of 10 MHz and an amplitude resolution of 12 bits. At the end
222 of the experiment, nearly 500 events have been detected according to this
223 protocol.

224 **3. Shear faulting and post-failure slip**

225 *3.1. Identification of the faulting dynamics*

226 The shale deformation experiment can be divided into an isotropic stress
227 loading (Phase 0), followed by a deviatoric stress loading. The deviatoric
228 loading stage itself is composed of three phases as discussed below (Figs. 4
229 and 5).

230 During Phase 0, the specimen reaches the simulated *in situ* stress con-
231 dition with a confining pressure of 10 MPa (point A in Figs. 4 and 5).
232 This phase consists of a step-wise increase of the confining pressure and an
233 equilibration of the specimen at the target condition over several days.

234 Phase 1 corresponds to the *shear faulting* (yellow area in Figs. 4 and 5).
235 Axial loading is applied to the specimen at a controlled vertical displacement
236 rate of 1 mm/h until the peak axial stress is slightly passed and a first
237 moderate stress drop of about 1 MPa is observed, most probably concomitant
238 with a first slip of the newly formed shear fault (point B in Figs. 4 and 5).
239 The dip angle of the slip surface with respect to a horizontal plane have
240 been estimated post mortem to be about 45°, coinciding approximately with
241 the orientation of the shale bedding. Such an orientation is expected as
242 it coincides with the plane of maximum shear stress in this axisymmetric
243 configuration (see failed sample in Fig. 3).

244 Phase 2 corresponds to the *slow fault slip* (blue area in Figs. 4 and 5). The
245 vertical displacement rate is maintained constant so that the newly formed
246 shear fault is slipping at constant rate, while the axial stress drop of about
247 7 MPa is more pronounced than in Phase 1.

248 Phase 3 corresponds to the *fast fault slip* (pink area in Figs. 4 and 5) The

249 vertical displacement rate is suddenly increased to 10 mm/h, which leads to
250 a sudden, moderate and temporary increase of the axial stress of less than 1
251 MPa (point C in Figs. 4 and 5). While the axial displacement is maintained
252 constant at that higher rate, after a temporary stabilisation, the axial stress
253 starts to slowly increase to reach a plateau by the end of the experiment
254 (point D in Figs. 4 and 5).

255 In addition to the evolution with time of the axial stress and displacement,
256 Figs. 4 and 5 also display the evolution of the micro-seismic activity in terms
257 of cumulated number of MSEs and rate of occurrence, respectively. Overall,
258 the cumulated number of events is linearly related to the axial displacement
259 rate, except temporarily after the increase in the imposed displacement rate
260 from 1 to 10 mm/hour and until the axial stress reaches a plateau. Con-
261 sistentlly, the rate of micro-seismic activity is strongly correlated with the
262 imposed displacement rate and the evolution of the axial stress. More de-
263 tails about this part of the dataset are provided in Section 4.3.

264 *3.2. Analysis of the stress-strain data*

265 At the end of the isotropic stress loading (Phase 0 aimed at reaching a
266 confining pressure of 10 MPa), Gages 1, 2, and 3 display a similar amount
267 of strain (0.123%), whereas Gage 4 (along the bedding and at 45° to the
268 specimen's axis) displays about half that amount of strain (0.072%). This
269 suggests a significant stress-induced anisotropy of the shale in which the bed-
270 ding direction is significantly less compliant than the three other measured
271 directions. However, the difference in the magnitude of the recorded strain
272 between Gages 1, 2 and 3 does not clearly reflect a larger compliance in a
273 direction orthogonal to the bedding compared to the two other intermediate

274 orientations (at 45° to the bedding). Over all, the amount of deformation
275 experienced by the specimen during this isotropic stress loading is relatively
276 small, which may explain the lack of sensitivity of the strain gauge recordings
277 and therefore the lack of discrimination between the three directions probed
278 by Gages 1, 2 and 3.

279 During the deviatoric stress loading, the four gauges record a significantly
280 larger amount of strain (Fig. 6). The whole dataset recorded during Phases
281 1, 2 and 3 is displayed in this figure. Note however that past the point
282 of strain localisation (shear faulting, slightly beyond the peak stress corre-
283 sponding to Point B in Fig. 4-6), the local strain measurement provided by
284 the strain gauges is no longer representative of the average strain field over
285 the volume of the specimen because most of the imposed axial displacement
286 is then accommodated by the slipping shear fault. The largest deformation is
287 expectedly recorded along the specimen's axis (about 1% at the peak stress,
288 along the maximum principal compressive stress), while the radial strain
289 along the minimum principal stress is negative due to Poisson's effect (about
290 -0.1% at the peak stress). Gages 3 and 4 record an intermediate amount of
291 strain, consistent with their orientation with respect to the principal stress
292 axes. The difference in magnitude of strain recorded by these two gauges
293 highlights again the existence of a significant anisotropy in the mechanical
294 compliance of the shale. Indeed, in view of their similar orientation with
295 respect to the principal compressive stress axis (45°), they should record a
296 similar deformation if the shale was isotropic. However, it turns out that
297 Gage 3 oriented normal to the bedding records a larger strain than gauge 4
298 oriented along the bedding due to the mechanical anisotropy of the shale.

299 These observations suggest that the quasi-static mechanical compliance
300 of this shale exhibits a significant directional dependency (anisotropy), that
301 is, the compliance across the bedding plane is measurably larger than that
302 along the bedding. This phenomenon has been extensively reported in the
303 literature for many shales of different origin and geological history (e.g., [11,
304 14, 40, 41, 42] and references therein). It has also been reported for other
305 sedimentary rocks (e.g., [10] and references therein). It is therefore reasonable
306 to assume that while subjected only to a confining pressure, this shale is
307 transversely isotropic (TI) in terms of mechanical properties with a symmetry
308 axis orthogonal to the bedding plane. This symmetry might not hold during
309 deviatoric stress loading because the applied axial stress does not coincide
310 with the shale’s original axis of transverse isotropy.

311 **4. Micro-seismic signature**

312 *4.1. Analysis of the P-wave velocity data*

313 The 21 P-wave velocity surveys recorded during the experiment were
314 processed with the *Insite* software. The flight time of the P-wave recorded
315 in each waveform is picked manually rather than by using an automatic
316 algorithm because of the reasonable number of acoustic surveys. This allows
317 systematic quality control of the results with a high degree of confidence.
318 For each source-receiver pair, the P-wave velocity V_p is calculated using
319 the shortest straight path between the transducers, that is from the closest
320 edge of each transducer to the other (known from the spatial location and
321 dimension of the transducers).

322 At a given stage of the experiment, the P-wave velocity along five direc-
323 tions of propagation are estimated, which are referred to as $V_p(90^\circ)$, $V_p(60^\circ)$,
324 $V_p(45^\circ)$, $V_p(30^\circ)$, and $V_p(0^\circ)$, where the angles in degrees indicate the prop-
325 agation direction with respect to the bedding plane. Note that for each nom-
326 inal ray path orientation θ with respect to the shale bedding, V_p is averaged
327 over all source-receiver pairs yielding a ray path orientation comprised in the
328 interval $[\theta-5^\circ, \theta+5^\circ]$.

329 The uncertainty in the estimation of the relative variation of V_p along a
330 given direction during the experiment is of the order of 1%. This estimate is
331 based on: (i) a waveform sampling period of $0.1 \mu s$ for a propagation time
332 within the specimen comprised between 10 and $15 \mu s$, and (ii) an uncertainty
333 in the determination of the propagation distance of about 0.1 mm (caliper) for
334 an average travel distance of about 30 mm. The uncertainty in the estimation
335 of the absolute value of V_p along a given direction is expected to be higher,
336 of the order of 10%, mainly due to the inherently higher uncertainty of about
337 $1 \mu s$ with which a human operator can decide for the P-wave arrival time
338 from an experimentally recorded waveform.

339 During the isotropic loading (Phase 0), and for all propagation direc-
340 tions, a significant increase in V_p with a confining pressure increase from
341 0 to 3 MPa is observed, with only slight increase between 3 and 10 MPa
342 (Fig. 7a). Despite the uncertainty in the estimation of the absolute value
343 of V_p (the worst case scenario is represented by the error bars in Fig. 7a),
344 the relative magnitudes of V_p along the different propagation directions can
345 be considered as reliable. The elastic anisotropy of the shale is clearly high-
346 lighted, with a slow $V_p(90^\circ)$ and a fast $V_p(0^\circ)$ velocity across and along the

347 bedding, respectively. We also observe that $V_p(60^\circ)$, $V_p(45^\circ)$ and $V_p(30^\circ)$
348 exhibit intermediate values, inversely proportional to their angular inclina-
349 tion with respect to the bedding plane. This suggests that the shale specimen
350 can reasonably be assumed to be transversely isotropic (TI) in terms of its
351 dynamic elastic response. This phenomenon has also been extensively re-
352 ported in the literature for many shales of different origin and geological
353 history (e.g., [40, 41] and references therein)

354 In view of the size of the ultrasonic transducers and the propagation
355 distances within the specimen, the estimated P-wave velocities are assumed
356 to be group (ray) velocities ([12]). However, along the symmetry axis and
357 the symmetry plane of the TI shale, group (ray) and phase velocity coincide.
358 Therefore, Thomsen's parameter [47] $\varepsilon = (V_p(0^\circ)^2 - V_p(90^\circ)^2)/2V_p(90^\circ)^2$
359 quantifying the P-wave anisotropy in a TI medium can be estimated using
360 the measured group velocities (Fig. 7b, d).

361 The P-wave velocity and the corresponding P-wave anisotropy as mea-
362 sured by Thomsen's ε parameter exhibit a significant dependency to the
363 confining pressure (Fig. 7a, b): ε drops from 1.8 to 0.8 between 0 and 3 MPa
364 and remains almost constant from 3 to 10 MPa. This suggests a closure
365 of pre-existing micro-cracks (damage) sub-parallel to the bedding with the
366 increase in effective pressure, which is consistent with the dependency of the
367 gas permeability to effective pressure reported in Section 2.1. In contrast,
368 during the deviatoric stress loading (Phases 1 to 3), P-wave velocities appear
369 nearly constant or rise slightly (Fig. 7c), and Thomsen's parameter ε exhibits
370 a moderate dependency to deviatoric stress (Fig. 7d), decreasing to 0.6 as
371 differential stress increases from 0 to 35 MPa.

372 *4.2. P-wave velocity model of the shale sample*

373 In order to spatially locate the MSEs recorded during the experiment,
374 a P-wave velocity model is required. Based on the analysis of the P-wave
375 velocity data, the velocity model should in principle account for the TI nature
376 of the elastic properties of the shale and the variation of the P-wave velocities
377 with stress. However, as the aim is only to locate MSEs recorded during the
378 deviatoric stress loading (Phases 1 to 3), and accounting for the fact that
379 the P-wave velocities are not significantly affected by the deviatoric stress
380 during these phases, the velocities recorded at the start of Phase 1 are used
381 to build the required velocity model of the shale, that is when the confining
382 pressure is 10 MPa and the axial stress is zero. Note that this model is only
383 an approximation assuming that the shale specimen is homogeneous.

384 In addition, because their spatial location is known, the ultrasonic sources
385 shot during the velocity surveys can first be used to assess the validity of both
386 the location (inversion) algorithm and the selected TI velocity model. A
387 Simplex algorithm implemented in the *Insite* software, and a velocity model
388 based on a slow velocity $V_p(90^\circ) = 2000$ m/s and an $\varepsilon = 0.78$ are used. The
389 orientation of the symmetry axis of this model is inferred from the known
390 orientation of the bedding in the specimen, that is at 45° to the specimen's
391 axis.

392 Although this velocity model accounts for the experimentally estimated
393 velocity and anisotropy, at the scale of the specimen used in this experiment,
394 this combination of values produced a distorted pattern of location of the
395 source shots. In an attempt to improve the results and optimise the pro-
396 cedure, several values of the slow velocity $V_p(90^\circ)$ and the value of ε are

397 tested. The combination that produces the best source shots locations is
398 found to be $V_p(90^\circ) = 1900$ m/s and $\varepsilon = 0.625$. The inversion using these
399 values and applied to 176 ultrasonic shots reflects reasonably well the known
400 position of the ultrasonic array, i.e. the sources clearly locate in the vicinity
401 of the transducers (Fig.8). The remaining mismatch between the recovered
402 and the actual sensor positions can reasonably be attributed to: (i) the pro-
403 gressive loss of transverse isotropy of the shale during the application of the
404 deviatoric stress (not aligned with the original symmetry axis); and (ii) the
405 heterogeneity of the velocity field in the natural shale specimen.

406 *4.3. Analysis of the induced micro-seismicity*

407 *4.3.1. Spatio-temporal evolution*

408 According to the passive monitoring protocol described in Section 2.3,
409 nearly 500 events are detected during the whole experiment, although not
410 all of them are identified as MSEs. Due to the reasonable number of events
411 recorded, a manual check of the acquired data set was possible. A number
412 of events are identified as electronic noise while others are discarded due to
413 the low SNR of the recorded waveforms. Finally, only the events that could
414 be reliably located within the volume of the specimen are selected for further
415 analysis (Fig. 9). This procedure finally leads to the selection of a total of
416 280 MSEs: 34 during Phase 1 (yellow spheres in Fig. 9), 14 during Phase 2
417 (blue spheres), and 232 during Phase 3 (pink spheres). The average location
418 error for the whole dataset is 3.5 mm. For an imposed axial displacement
419 of 1 mm/hour (Phase 2), the average rate of MSEs is 0.07 MSE/second.
420 This value reaches an average of 0.19 MSE/second over the whole Phase 3
421 of imposed axial displacement at 10 mm/hour. Note that only 15 events

422 are detected during Phase 0 of confining pressure loading applied to reach
423 the simulated *in situ* stress. For sake of clarity and because they are not
424 induced by the triaxial loading, these events have been discarded and are
425 not represented in (Fig. 9).

426 The spatial distribution of the MSEs is clearly not random: they appear
427 distributed along two main planar structures, sub-parallel to the shale bed-
428 ding (Fig. 10). A first structure, highlighted as a yellow plane, is initiated
429 during Phase 1: few yellow MSEs seem to be distributed over the volume
430 of the specimen, but most of them appear to cluster along the highlighted
431 yellow plane. This reflects an initial diffuse damage, then a first pattern of
432 strain localisation in the vicinity of the yellow plane. The second structure,
433 highlighted as a pink plane, is initiated during Phase 2 (slow slip, blue MSEs)
434 and largely develops during Phase 3 (fast slip, pink MSEs). Note however
435 that the MSEs occurring during Phase 3 do not locate only in the vicinity
436 of the pink plane, but also in the overlap volume between the yellow and
437 pink planes, and on the yellow plane to a lesser extent. In addition, there
438 are few yellow MSEs located on the pink plane, which suggests that shear
439 faulting could have been initiated simultaneously on both planes, then the
440 upper shear plane takes over the lower one and accommodates most of the
441 rock shortening but the end of the experiment.

442 The above results are derived from the combined use of active ultrasonic
443 and passive MS monitoring of the deformation process. Both monitoring
444 techniques are based only on the picking of the time of arrival of the first
445 phase in the recorded waveforms.

446 *4.3.2. Moment tensor analysis*

447 The first motion polarities and relative amplitudes of the waveforms
448 recorded for a given MSE can be used to estimate its source mechanism,
449 similar to the approach widely used in seismology to define the source mech-
450 anism of earthquakes. This method, generally known as the Moment Tensor
451 Inversion (MTI), is implemented in the *Insite* software and is used here to
452 characterise the focal mechanism of the recorded MSEs [37, 52, 53, 54]. How-
453 ever, in order to obtain reliable MTI results, the analysis must be restricted
454 to MSEs of sufficiently high quality, which represent a relatively small subset
455 of all the spatially located MSEs. The MTI has been carried out on all the
456 MSEs located spatially. The results reported Figure 11 fulfil the additional
457 criteria: (i) a spatial location error strictly lower than 5 mm; (ii) a mean
458 error factor lower than 17; (iii) an inversion quality index lower than 4.4;
459 and (iii) a T-k error norm lower than 0.3. The mean error factor measures
460 the difference between the amplitude residual and the estimated uncertainty
461 in the original amplitude measurement. The inversion quality factor is based
462 on the 6x6 covariance matrix and depends on the Green's functions used,
463 rather than the amplitudes. It is computed from the sum of the squares of
464 the elements of the covariance matrix. The T-k error norm is the RMSE of
465 the errors on the deviatoric (T) and isotropic (k) parameters representing the
466 source [23]. The threshold values of the mean error factor, inversion quality
467 index and T-k error norm have been selected as the mean values obtained for
468 the whole set of spatially located MSEs to which the MTI has been carried
469 out. With such criteria, 42 MSEs have been selected: 11 MSEs in Phase
470 1, 6 MSEs in Phase 2 and 25 in Phase 3. The average amplitude residual

471 parameter for these 42 MSEs is 0.21, and the standard deviation is 0.08.

472 Figure 11 shows the spatial distribution of the 42 MSEs within the shale
473 specimen. For each MSE, the detecting ultrasonic sensors covered a reason-
474 able portion of the solid angle around it, which allowed for a reliable MTI. In
475 this figure, MSEs #79 in Phase 1, #128 in Phase 2 and #259 in Phase 3 have
476 been highlighted because they exhibit the largest location magnitude for each
477 phase. For each of these three MSEs, the focal mechanism is represented by a
478 focal sphere plot, i.e., the so-called *beachballs* widely used in seismology. The
479 sensors that detected the MSE are represented by small discs in the *beach-*
480 *balls*, with the convention that black and white discs represent compressional
481 and dilatational first motion, respectively. The fault plane is calculated using
482 the first-motion polarity of the P-wave picked in the waveform recorded by
483 each sensor that detected this MSE and is represented by red circles in each
484 focal sphere plot. The orientation of the fault plane is consistent with that of
485 the fault planes identified statistically by the spatial distribution of the MSEs
486 and by the post-mortem observation of the sample.

487 The MTI procedure yields the focal mechanism of each MSE as a combi-
488 nation of three basic modes, with usually a dominant mode: ISO, stands for
489 isotropic dilatation, DC for double-couple (shear), and CLVD for compen-
490 sated linear vector dipole [44, 52]. Hudson’s so-called T-k plot ([23]) is well-
491 suited to display such decomposition in an equal-area graph (Fig. 11) where
492 the T-axis stands for the deviatoric component of the mechanism (shear
493 deformation) and k stands for the normal/isotropic component (volumetric
494 deformation, either positive-explosive or negative-implosive).

495 Figure 13 reports graphically the results of the moment tensor decom-

496 position of the selected high quality MSEs. The top graph shows the de-
497 tailed decomposition into DC, CLVD and ISO MSEs; the lower graph shows
498 the simpler decomposition into shear (DC) and non-shear (ISO+CLVD)
499 MSEs. These plots suggest a transition from non-shear dominated to shear-
500 dominated micro-seismic activity when the rock evolves from initial failure
501 to larger and faster slip along the fault

502 **5. Discussion**

503 *5.1. Shear faulting in the laboratory and relay ramp structures in the field*

504 The post-mortem picture of the failed specimen and the location of the
505 recorded MSEs are in good agreement (see Fig. 10). Although the picture
506 of the specimen cannot show the internal structure of the shear faults, their
507 emergence at the external boundary of the specimen is in agreement with the
508 location of the MSEs at this boundary. Two different planar structures are
509 identified from the spatio-temporal location of the 280 MSEs (Figs. 9 and
510 10).

511 These results suggest that the lower shear fault (yellow plane) is most
512 active (accommodates most of the imposed axial displacement) at the early
513 stages after strain localisation (Phase 1), although few yellow events are
514 already located on the top part of the upper shear fault. However, during
515 this phase no clustering of MSE is observed on this upper plane. During
516 Phase 2, a transition of the micro-seismic activity is observed from the lower
517 shear fault toward the upper shear fault (pink plane). During Phase 3 most
518 of the imposed axial displacement is accommodated by the upper shear fault,
519 although few events are still located on the lower shear fault, indicating that

520 it is not entirely inactive. This is consistent with the sequence of events
521 associated with a typical relay ramp structure formed during the growth of
522 normal fault systems in large scale geology

523 This upward transition from the lower to the upper SF is particularly
524 visible in Figure 10 where the MSEs in each phase have been colour-coded
525 according to their time of occurrence within the phase. More precisely, once
526 the yellow SF is formed and its activity slows down at the end of Phase
527 1, the blue MSEs of Phase 2 first appear at the lower end of the pink SF
528 then the MS activity migrates upward along this SF and approaches the
529 boundary of the specimen. Once the pink SF is largely developed, part of
530 the MS activity (pink MSEs) locates in the overlap volume between the two
531 SF planes. In summary, it seems that the lower shear fault forms first (yellow
532 plane), before the micro-seismic activity (blue spheres) migrates upward and
533 the the upper shear fault forms and accommodates most of the subsequently
534 imposed axial displacement (pink plane). This is essentially similar to typical
535 sequence of events associated with either (i) the formation of a relay ramp
536 structure during the growth of normal fault systems in large scale geology;
537 or (ii) fractures growing towards one another and overlapping.

538 *5.2. Silent failure, slow slip and slip rate dependency*

539 Phase 1 is quasi-aseismic (only 34 MSEs), at least in the 0.5 MHz range
540 of sensitivity of the ultrasonic transducers used in the experiment (about 0.1
541 to 1 MHz). This is surprising because Phase 1 corresponds to the failure of
542 the clay-rich rock and contrasts with other sedimentary or crystalline rocks
543 (e.g., sandstones, granites) for which large amounts of precursory MSEs are
544 usually recorded prior to the macroscopic failure, and failure itself has been

545 reported to generate a much stronger MS activity (thousands of events).
546 Phase 2 of slow slip on the yellow shear fault induces very small amount of
547 MS activity: clays might be acting as a ?lubricant? on the fault(s) at that slip
548 rate. Silent or almost silent failures have already been reported in materials
549 being deformed close to the brittle ductile transition, for instance Carrara
550 marble [43], or Volterra gypsum at room temperature [5]. In all cases, ?silent?
551 failures are accompanied by slow slip and stress drop, i.e. the macroscopic
552 fault releases the stress too slowly for the rupture and the slip to accelerate
553 and start radiating elastic waves. As such, slow failures can be viewed as
554 quasi-static failures in the Griffith sense, i.e., the entire energy release rate is
555 dissipated at the rupture tip into fracture surface, damage and plastic strain.
556 Note that slow failures are not always silent, because at the microscopic
557 scale, damage at the crack tip can actually also radiate elastic waves and
558 be associated to MSEs, as for instance during quasi static fault growth in
559 granite [33], slow failure in porous basalt [4] or shear or compaction band
560 formation in sandstones [15, 17]. Hence, both the growth of macroscopic
561 fracture and the accumulation of microscopic damage are ?silent? in the
562 frequency range investigated in these experiments. This suggests that shale
563 and clays are indeed potential good candidate to host slow slip within shallow
564 accretionary prism [19, 22], or in the shallow section of continental faults [50].

565 In contrast, Phase 3 of slip acceleration from 1mm/h to 10mm/h, i.e.
566 slip slip velocities slightly larger than that observed during slow earthquakes
567 which are typically of the order of several tens of cm per year only [20], gen-
568 erates a significant amount of MS activity. During that fast slip phase, the
569 AE rate and the slip are proportional so there seems to be a significant rate

570 dependency of the lubrication potential of clays. In Figure 13, the slip ac-
571 celeration triggers an instantaneous increase in the friction coefficient, which
572 is typical of the direct effect [35]. After that, the fault first weakens with
573 increasing slip, then starts to re-strengthen after a few millimetres of slip,
574 exhibiting thus the typical velocity strengthening behaviour observed for clay
575 minerals [38]. It is interesting to note that during that phase, nevertheless,
576 numerous MSEs are observed, probably linked to the dynamic shear failure
577 of small asperities on the fault plane, as demonstrated by the inverted focal
578 mechanisms (see Fig 11). These observations highlight the possible interac-
579 tions between small asperities and slow slip of a velocity-strengthening fault
580 [3], which could be considered as a realistic experimental analogue of natural
581 observations of non-volcanic tremors and (very) low-frequency earthquakes
582 triggered by slow slip events [19, 21].

583 **6. Conclusion**

584 We have demonstrated that it is possible to apply laboratory techniques
585 usually employed for monitoring micro-seismicity on reservoir or crystalline
586 rocks to anisotropic shale specimens. The data acquired during this triaxial
587 experiment allowed us (i) to quantify the P-wave (dynamic) anisotropy of
588 the shale and its evolution with stress; (ii) monitor the micro-seismic activ-
589 ity occurring during failure and subsequent fault slip at two different rates.
590 The gas permeability as well as the P-wave velocity data and their respective
591 sensitivity to pressure suggest the existence of micro-cracks in this partially
592 dry shale specimen at room conditions. although these micro-cracks tend to
593 close with increasing effective confining pressure. The spatio-temporal loca-

594 tion of the MSEs recorded during the three phases of the experiment (failure,
595 slow fault slip, fast fault slip) indicates that two shear fault planes where in
596 competition after the initial strain localisation that occurred near the peak
597 axial stress. The evolution of these two shear fault planes as derived from the
598 micro-seismic monitoring is consistent with the sequence of events associated
599 with a typical relay ramp structure formed during the growth of normal fault
600 systems in large scale geology. The moment tensor inversion carried out on
601 the highest quality MSEs suggests a transition from non-shear dominated
602 to shear-dominated micro-seismic activity when the rock evolves from initial
603 failure to larger and faster slip along the fault. The spatial orientation of the
604 fault plane obtained on the highest magnitude MSE for each phase is con-
605 sistent with the macroscopic orientation of the shear faults. The frictional
606 behaviour of the shear faults highlights the possible interactions between
607 small asperities and slow slip of a velocity-strengthening fault, which could
608 be considered as a realistic experimental analogue of natural observations of
609 non-volcanic tremors and (very) low-frequency earthquakes triggered by slow
610 slip events.

611 **Acknowledgments**

612 This research work was sponsored by BP under the contract number
613 BPO-06-01329. This support is gratefully acknowledged.

614 **References**

- 615 [1] Amitrano D., Brittle-ductile transition and associated seismicity:
616 Experimental and numerical studies and relationship with the
617 b value, *Journal of Geophysical Research-Solid Earth*, **108**(B1),
618 doi:10.1029/2001JB000680, 2003.
- 619 [2] Amann F., Button E.A., Evans K.F., Gischig V.S., and Blümel M., Ex-
620 perimental study of the brittle behavior of clay shale in rapid unconfined
621 compression, *Rock Mechanics and Rock Engineering*, **44**, 415 - 430, 2011.
- 622 [3] Ariyoshi K., Hori T., Ampuero J.P., Kaneda Y., Matsuzawa T., Hino R.
623 and Hasegawa A., Influence of interaction between small asperities on
624 various types of slow earthquakes in a 3-D simulation for a subduction
625 plate boundary, *Gondwana Research*, **16**, 534 - 544, 2009.
- 626 [4] Benson P.M., Thompson B.D., Meredith P.G., Vinciguerra S. and Young
627 R.P., Imaging slow failure in triaxially deformed Etna basalt using 3D
628 acoustic emission location and X-ray computed tomography, *Geophys-
629 ical Research Letters*, **34**(3), 2007.
- 630 [5] Brantut N., Schubnel A. and Guéguen Y., Damage and rupture dynam-
631 ics at the brittle-ductile transition: The case of gypsum, *Journal of
632 Geophysical Research-Solid Earth*, **116**(B1), 1978 - 2012, 2011.
- 633 [6] Chang S.-H., and Lee C.-I., Estimation of cracking and damage mecha-
634 nisms in rock under triaxial compression by moment tensor analysis of
635 acoustic emission, *International Journal of Rock mechanics and Mining
636 Sciences*, **41**, 1069 - 1086, 2004.

- 637 [7] Charalampidou E.-M., Hall S.A., Stanchits S., Lewis H., and Viggiani
638 G., Characterization of shear and compaction bands in a porous sand-
639 stone deformed under triaxial compression, *Tectonophysics*, **503**, 8 - 17,
640 2011.
- 641 [8] Charalampidou E.-M., Stanchits S., Kwiatek G., and Dresen G., Brittle
642 failure and fracture reactivation in sandstone by fluid injection, *European*
643 *Journal of Environmental and Civil Engineering*, **19**, 564 - 579, 2015.
- 644 [9] Dautriat J., Sarout J., David C., Bertauld D., and Macault R., Remote
645 monitoring of the mechanical instability induced by fluid substitution
646 and water weakening in the laboratory, *Physics of the Earth and Plan-*
647 *etary Interiors, This issue*.
- 648 [10] David C., Dautriat D., Sarout J., Delle Piane C., Menéndez B., Macault
649 R., and Bertauld D., Mechanical instability induced by water weakening
650 in laboratory fluid injection tests, *Journal of Geophysical Research-Solid*
651 *Earth*, **120**, 4171 - 4188, doi:10.1002/ 2015JB011894.
- 652 [11] Delle Piane C., Dewhurst D.N., Siggins A.F. and Raven M., Stress-
653 induced anisotropy in brine saturated shale, *Geophysical Journal Inter-*
654 *national*, **184**, 897 - 906, 2011.
- 655 [12] Dellinger J., and Vernik L., Do travel times in pulse transmission ex-
656 periments yield anisotropic group or phase velocities?, *Geophysics*, **41**,
657 1774 - 1779, 1994.
- 658 [13] Dewhurst D.N. and Siggins A.F., Impact of fabric, microcracks and

- 659 stress field on shale anisotropy, *Geophysical Journal International*, **165**,
660 135 - 148, 2006.
- 661 [14] Dewhurst D.N., Siggins A.F., Sarout J. and Raven M., Geomechanical
662 and ultrasonic characterization of a Norwegian Sea shale, *Geophysics*,
663 **76**, WA101 - WA111, 2011.
- 664 [15] Fortin J., Stanchits S., Dresen G., and Gueguen Y., Acoustic emission
665 and velocities associated with the formation of compaction bands in
666 sandstone, *Journal of Geophysical Research-Solid Earth*, **111**, B10203,
667 doi:10.1029/2005JB003854, 2006.
- 668 [16] Fortin J., Stanchits S., Dresen G., and Gueguen Y., Damage evolution,
669 acoustic emissions and elastic wave velocities in porous carbonate rocks,
670 *AGU Fall Meeting Abstracts*, #T23D-0539, 2009.
- 671 [17] Fortin J., Stanchits S., Dresen G., and Gueguen Y., Acoustic emissions
672 monitoring during inelastic deformation of porous sandstone: Compar-
673 ison of three modes of deformation, *Pure and Applied Geophysics*, **166**,
674 823 - 841, 2009.
- 675 [18] Guglielmi Y., Cappa F., Avouac J.-P., Henry P., and Elsworth D., Seis-
676 micity triggered by fluid injection-induced aseismic slip, *Science*, **348**,
677 1224 - 1226, 2015.
- 678 [19] Hirose H., Asano Y., Obara K., Kimura T., Matsuzawa T., Tanaka S.
679 and Maeda T., Slow earthquakes linked along dip in the Nankai subduc-
680 tion zone, *Science*, **330**, 1502 - 1502, 2010.

- 681 [20] Ikari M.J., Ito Y., Ujiie K. and Knopf A.J., Spectrum of slip behaviour
682 in Tohoku fault zone samples at plate tectonic slip rates, *Nature Geo-*
683 *sciences*, 2015.
- 684 [21] Ito Y., Obara K., Shiomi K., Sekine S. and Hirose H., Slow earthquakes
685 coincident with episodic tremors and slow slip events, *Science*, **315**, 503
686 - 506, 2007.
- 687 [22] Ito Y., Hino R., Kido M., Fujimoto H., Osada Y., Inazu D. and Mishina
688 M., Episodic slow slip events in the Japan subduction zone before the
689 2011 Tohoku-Oki earthquake, *Tectonophysics*, **600**, 14 - 26, 2013.
- 690 [23] Hudson J.A., Pearce R.G. and Rogers R.M., Source type plot for inver-
691 sion of the moment tensor, *Journal of Geophysical Research-Solid Earth*,
692 **91**, 765 - 774, 1989.
- 693 [24] Johnston J.E. and Christensen N.I., Seismic anisotropy of shales, *Jour-*
694 *nal of Geophysical Research-Solid Earth*, **100**(B4, 5991 - 6003, 1995.
- 695 [25] Josh M., Esteban L., Delle Piane C., Sarout J., Dewhurst D.N. and
696 Clennell M.B., Laboratory characterisation of shale properties, *Journal*
697 *of Petroleum Science and Engineering*, **88-89**, 107 - 124, 2012.
- 698 [26] Kusunose K., Lei X., Nishizawa O. and Satoh T., Effect of grain size on
699 fractal structure of acoustic emission hypocenter distribution in granitic
700 rock, *Physics of the Earth and Planetary Interiors*, **67**, 194 - 199, 1991.
- 701 [27] Le Gonidec Y., Sarout J., Wassermann J. and Nussbaum C., Dam-
702 age initiation and propagation assessed from stress-induced microseismic

- 703 events during a mine-by test in the Opalinus Clay, *Geophysical Journal*
704 *International*, **198**, 126 - 139, 2014.
- 705 [28] Lei X., Kusunose K., Satoh T. and Nishizawa O., The hierarchical rup-
706 ture process of a fault: an experimental study, *Physics of the Earth and*
707 *Planetary Interiors*, **137**, 213 - 228, 2003.
- 708 [29] Lei X., Masuda K., Nishizawa O., Jouniaux L., Liu L., Ma W., Satoh T.
709 and Kusunose K., Detailed analysis of acoustic emission activity during
710 catastrophic fracture of faults in rock, *Journal of Structural Geology*,
711 **26**, 247 - 258, 2004.
- 712 [30] Lei X., Nishizawa O., Kusunose K., Cho A., Satoh T. and Nishizawa O.,
713 Compressive failure of mudstone samples containing quartz veins using
714 rapid AE monitoring: the role of asperities, *Tectonophysics*, **328**, 329 -
715 340, 2000.
- 716 [31] Lei X. and Satoh T., Indicators of critical point behavior prior to rock
717 failure inferred from pre-failure damage, *Tectonophysics*, **431**, 97 - 111,
718 2007.
- 719 [32] Lockner D.A., The role of acoustic emission in the study of rock fracture,
720 *International Journal of Rock Mechanics and Mining Sciences*, **30**, 883
721 - 899, 1993.
- 722 [33] Lockner D.A., Byerlee J.D., Kuksenko V., Ponomarev A. and Sidorin A.,
723 Quasi-static fault growth and shear fracture energy in granite, *Nature*,
724 **350**, 39 - 42, 1991.

- 725 [34] Lowry A.R., Larson K.M., Kostoglodov V. and Bilham R., Transient
726 fault slip in Guerrero, southern Mexico, *Geophysical Research Letters*,
727 **28**, 3753 - 3756, 2001.
- 728 [35] Marone C., Laboratory-derived friction laws and their application to
729 seismic faulting, *Annual Review of Earth and Planetary Sciences*, **26**,
730 643 - 696, 1998.
- 731 [36] Niemeijer A.R. and Spiers C.J., Influence of phyllosilicates on fault
732 strength in the brittle-ductile transition: insights from rock analogue
733 experiments, *Special publication-Geological Society of London*, **245**, 303,
734 2005.
- 735 [37] Pettitt W.S., Baker C., Young R.P., Dahlstrm L.-O. and Ramqvist G.,
736 The assessment of damage around critical engineering structures using
737 induced seismicity and ultrasonic techniques, *Pure and Applied Geo-*
738 *physics*, **159**, 179 - 195, 2002.
- 739 [38] Safer D.M. and Marone C., Comparison of smectite-and illite-rich gouge
740 frictional properties: application to the updip limit of the seismogenic
741 zone along subduction megathrusts, *Earth and Planetary Science Let-*
742 *ters*, **215**, 219 - 235, 2003.
- 743 [39] Sarout J., Delle Piane C., Nadri D., Esteban L. and Dewhurst D.N.,
744 A robust experimental determination of Thomsen's δ parameter, *Geo-*
745 *physics*, **80**, A19 - A24, 2015.
- 746 [40] Sarout J., Esteban L., Delle Piane C., Maney B. and Dewhurst D.N.,

- 747 Elastic anisotropy of Opalinus Clay under variable saturation and tri-
748 axial stress, *Geophysical Journal International*, **198**, 1662 - 1682, 2014.
- 749 [41] Sarout J. and Guéguen Y., Anisotropy of elastic wave velocities in de-
750 formed shales: Part 1—Experimental results, *Geophysics*, **73**, D75 - D89,
751 2008.
- 752 [42] Sarout J., Molez L., Guéguen Y. and Hoteit N., Shale dynamic proper-
753 ties and anisotropy under triaxial loading: Experimental and theoretical
754 investigations, *Physics and Chemistry of the Earth*, **32**, 896 - 906, 2007.
- 755 [43] Schubnel A., Walker E., Thompson B.D., Fortin J., Guéguen Y. and
756 Young R.P., Transient creep, aseismic damage and slow failure in Car-
757 rarra marble deformed across the brittle?ductile transition, *Geophysical*
758 *Research Letters*, **33**(17), 2006.
- 759 [44] Šílený J. and Milev A., Source mechanism of mining induced seismic
760 events: Resolution of double couple and non double couple models,
761 *Tectonophysics*, **456**, 3 - 15, 2008.
- 762 [45] Stanchits S., Mayr S., Shapiro S. and Dresen G., Fracturing of porous
763 rock induced by fluid injection, *Tectonophysics*, **503**, 129 - 145, 2011.
- 764 [46] Talebi S., Boone T.J. and Eastwood J.E., Injection-induced microseis-
765 micity in Colorado shales, *Pure and Applied Geophysics*, **153**, 95 - 111,
766 1998.
- 767 [47] Thomsen L., Weak elastic anisotropy, *Geophysics*, **51**, 1954 - 1966, 1986.

- 768 [48] Vernik L. and Liu X., Velocity anisotropy in shales: A petrophysical
769 study, *Geophysics*, **62**, 521 - 532, 1997.
- 770 [49] Warpinski N.R., Du J. and Zimmer U., Measurements of hydraulic-
771 fracture-induced seismicity in gas shales, *Society of Petroleum Engi-
772 neers*, **27**, SPE-151597-PA, doi:10.2118/151597-PA, 2012.
- 773 [50] Wei M. and Kaneko Y., Liu Y. and McGuire J.J., Episodic fault creep
774 events in California controlled by shallow frictional heterogeneity, *Nature
775 Geoscience*, **6**, 566-570, 2013.
- 776 [51] Wong T.F. and Baud P., The brittle-ductile transition in porous rock:
777 A review, *Journal of Structural Geology*, **44**, 25-53, 2012.
- 778 [52] Young R.P., Hazzard J.F. and Pettitt W.S., Seismic and micromechan-
779 ical studies of rock fracture, *Geophysical Research Letters*, **27**, 1767 -
780 1770, 2000.
- 781 [53] Young R.P. and Collins D.S., Seismic studies of rock fracture at the
782 underground research laboratory, Canada, *International Journal of Rock
783 Mechanics and Mining Sciences*, **38**, 787 - 799, 2001.
- 784 [54] Young R.P., Collins D.S., Reyes-Montes J.M. and Baker C., Quantifi-
785 cation and interpretation of acoustic emission and microseismicity at
786 the underground research laboratory, Canada, *International Journal of
787 Rock Mechanics and Mining Sciences*, **41**, 1317 - 1327, 2004.

Table 1: Nitrogen gas permeability of the partially saturated shale measured at three effective pressure states using a steady state method

Confining pressure (MPa)	Pore pressure (MPa)	Effective pressure (MPa)	Permeability $\times 10^{-19} \text{ m}^2$	Permeability $\times 10^{-7} \text{ mD}$
10	6	4	211	213
50	15	35	28.3	28.7
80	15	65	6.8	6.9

789 **List of Figures**

790 1 Experimental setup including (clockwise from top left): the
791 triaxial stress vessel; the rock specimen enclosed in a flexible
792 *Viton* sleeve, instrumented with 16 ultrasonic P-wave trans-
793 ducers and connected to 16 pulser-amplifiers and 4 strain gages;
794 the strain monitoring computer; and the ultrasonic/micro-
795 seismic monitoring computer. 43

796 2 Spatial location of the ultrasonic sensors represented around
797 the cylindrical shale specimen (right panel), and in an an-
798 tipodal equal-angle projection (left panel). Two ultrasonic
799 transducers became inoperative at the early stages of the ex-
800 periment (represented in red). The four strain gages attached
801 to the shale sample are also represented. 44

802 3 Triaxial loading path: (i) confining pressure loading to reach
803 the simulated in situ stress state of 10 MPa (green line); (ii)
804 axial loading up to the peak stress (36.77 MPa) and stress
805 drop (30.36 MPa) at a constant axial displacement rate of
806 1 mm/hour (plain red line); (iii) axial loading at a constant
807 displacement rate of 10 mm/hour during which the axial stress
808 variation is non monotonic (sudden increase to 31.09 MPa,
809 slower decrease to 29.92 MPa, then even slower increase to
810 reach a plateau at 32.82 MPa. The failed specimen obtained
811 after the experiment is pictured on the right hand side. 45

812 4 Evolution with time of the total axial and radial stresses, axial
813 displacement and cumulative number of micro-seismic events
814 during Phases 1 (A to B in yellow), 2 (B to C in blue) and 3
815 (C to D in pink) of the experiment. Over all, the cumulative
816 number of events is linearly related to the axial displacement
817 rate, except temporarily after the increase in the imposed dis-
818 placement rate from 1 to 10 mm/hour and until the axial stress
819 reaches a plateau. 46

820 5 Evolution with time of the total axial and radial stresses, axial
821 displacement and rate of micro-seismic activity during Phase
822 1 (A to B in yellow), 2 (B to C in blue) and 3 (C to D in
823 pink) of the experiment. The rate of micro-seismic activity
824 (amplitude of the green curve) is strongly correlated with the
825 imposed displacement rate (slope of the blue cuve in the lower
826 graph) and the evolution of the axial stress (amplitude of the
827 blue curve in the upper graph). 47

828 6 Stress-strain data during Phase 1 (A to B), 2 (B to C) and 3 (C
829 to D) of the experiment. The orientation of the strain gauges
830 with respect to the shale bedding and the specimen's axis are
831 also shown. The strain recorded by the gauges illustrates the
832 mechanical anisotropy of the shale. 48

833 7 Evolution of P-wave group (ray) velocity and anisotropy (Thom-
834 sen’s ϵ parameter) with confining pressure and deviatoric load-
835 ing. P-wave velocity data are indicated with a 10% error bar
836 (+/- 5%). The magnitude of the P-wave velocity as a func-
837 tion of the propagation direction with respect to the bedding
838 illustrates the elastic anisotropy of the shale. This anisotropy
839 decreases significantly with increasing confining pressure, and
840 is virtually not sensitive to the axial stress, at least until the
841 strain localises in a shear fault and the specimen fails. The
842 non-linear variation of the P-wave velocity with confining pres-
843 sure up to about 4 MPa suggests the existence of damage in
844 the shale specimen at room pressure; the linear variation of the
845 P-wave velocity with confining pressure above 4 MPa suggests
846 the existence of intrinsic anisotropy, most likely associated the
847 preferred alignment of clay platelets/particles. 49

848 8 Spatial and temporal location of the ultrasonic sources shot
849 during the velocity surveys. The squares represent the nominal
850 position of the centre of the ultrasonic sensors; the spheres
851 represent the location of the sources obtained by inversion
852 using the selected velocity model. 50

853 9 Spatial and temporal location of the micro-seismic events recorded
854 during the three phases of the deviatoric loading: in yellow
855 for Phase 1; in blue for Phase 2; and in pink for Phase 3.
856 The micro-seismic activity suggests the existence of two over-
857 lapping shear fault planes. Part of the micro-seismic activity
858 locates in the overlap volume between these two planes. A fea-
859 ture similar to relay ramps observed in large scale structural
860 geology. 51

861 10 Spatial and temporal location of the recorded MSEs separated
862 into the three phases of the experiment. For each phase, the
863 color of each event is scaled to its time of occurrence, i.e., first
864 events of the phase in green and last events in red. These
865 results suggest that the lower shear fault (yellow plane) is
866 most active (accommodates most of the imposed axial dis-
867 placement) at the early stages after strain localisation (Phase
868 1). During Phase 2, a transition of the micro-seismic activ-
869 ity is observed from the lower shear fault toward the upper
870 shear fault (pink plane). During Phase 3 most of the imposed
871 axial displacement is accommodated by the upper shear fault
872 although few events are still located on the lower shear fault,
873 indicating that it is not entirely inactive. This is consistent
874 with the sequence of events associated with a typical relay
875 ramp structure formed during the growth of normal fault sys-
876 tems in large scale geology. 52

877	11	Spatial location, T-k decomposition in Hudson's diagram [23],	
878		and moment tensor solution of the MSE with largest magni-	
879		tude in each of the three phases of the experiment: MSE #79	
880		in Phase 1, MSE #128 in Phase 2 and MSE #259 in Phase 3.	53
881	12	Results of the moment tensor decomposition of the selected	
882		high quality MSEs. The top plot shows the detailed decom-	
883		position into DC, CLVD and ISO MSEs; the lower plot shows	
884		the simpler decomposition into shear and non-shear MSEs (see	
885		main text for details).	54
886	13	Fault frictional behaviour and MS activity during Phases 2	
887		and 3. The fault slip is calculated from the measured post-	
888		failure axial displacement and the orientation of the fault plane	
889		determined post mortem to be approximately at 45° to the	
890		specimen's axis.	55

891 **Figures**

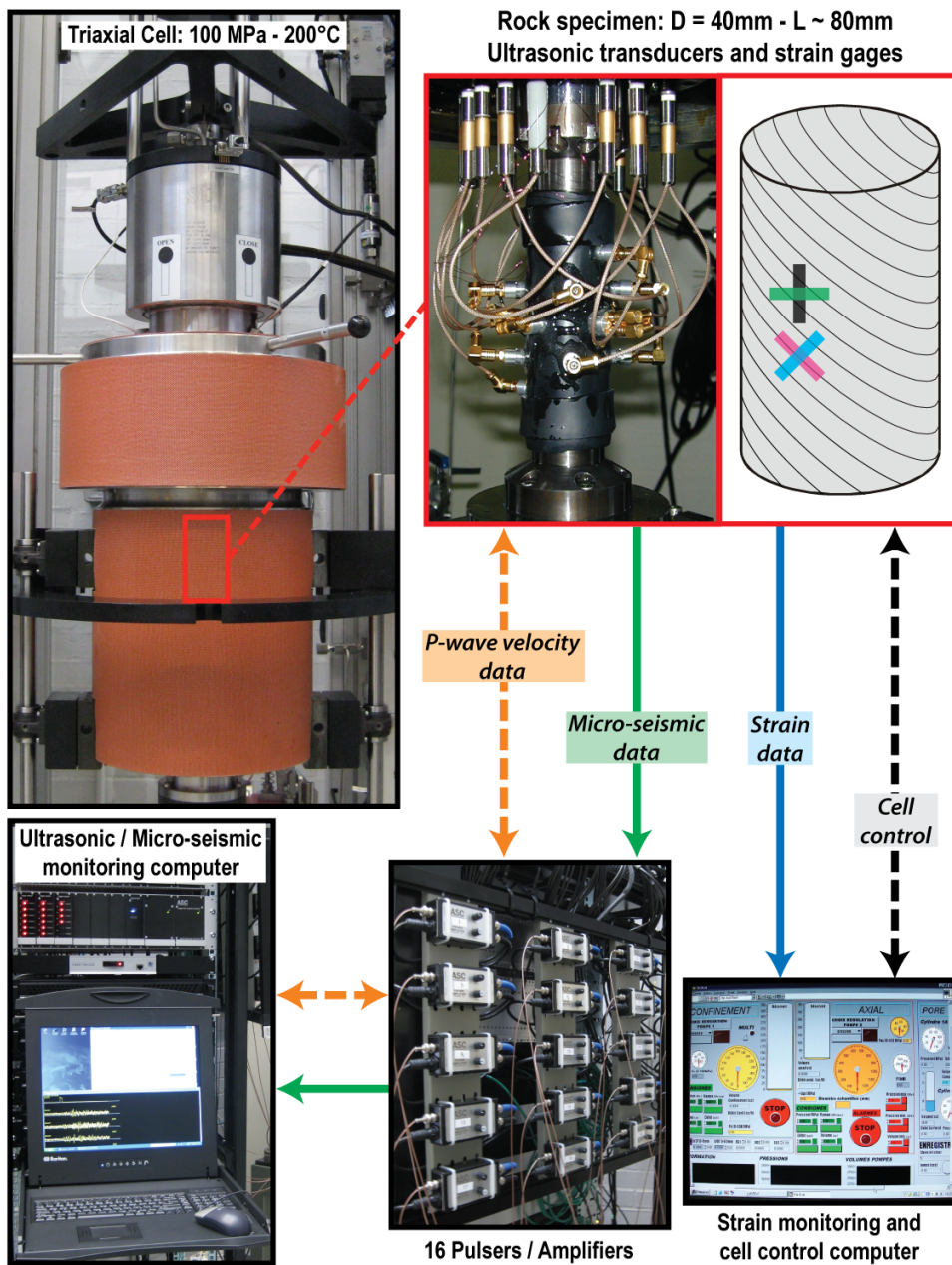


Figure 1: Experimental setup including (clockwise from top left): the triaxial stress vessel; the rock specimen enclosed in a flexible *Viton* sleeve, instrumented with 16 ultrasonic P-wave transducers and connected to 16 pulser-amplifiers and 4 strain gages; the strain monitoring computer; and the ultrasonic/micro-seismic monitoring computer.

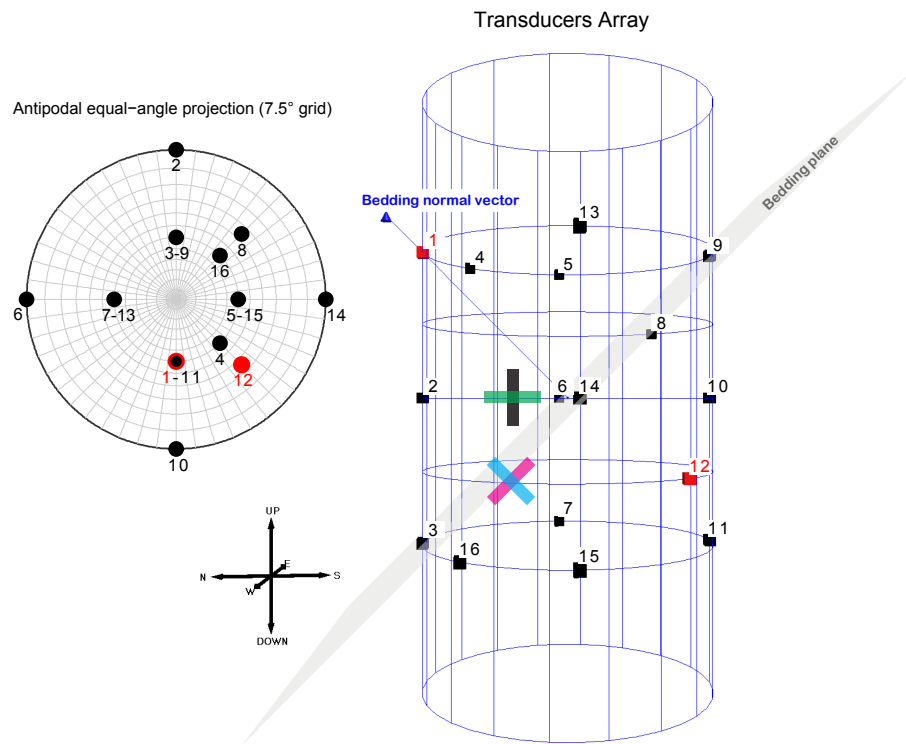


Figure 2: Spatial location of the ultrasonic sensors represented around the cylindrical shale specimen (right panel), and in an antipodal equal-angle projection (left panel). Two ultrasonic transducers became inoperative at the early stages of the experiment (represented in red). The four strain gauges attached to the shale sample are also represented.

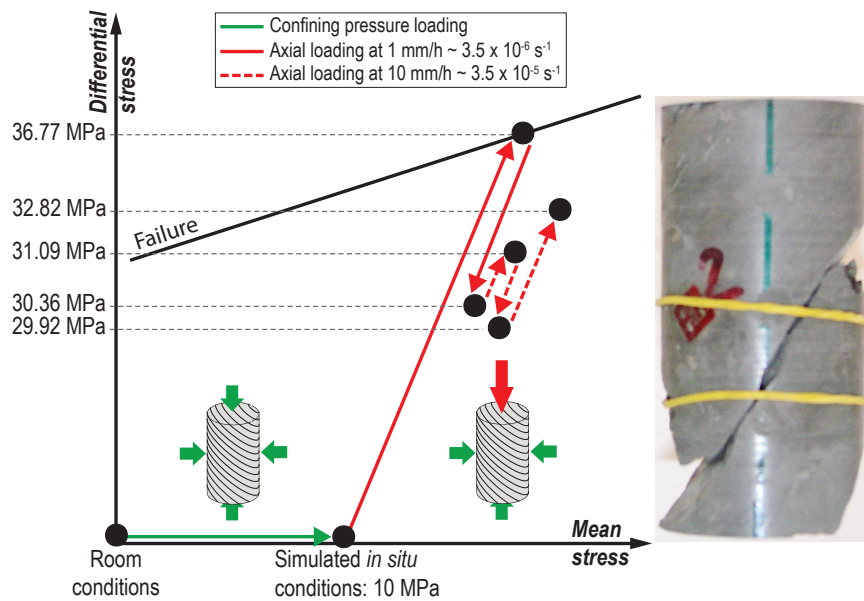


Figure 3: Triaxial loading path: (i) confining pressure loading to reach the simulated in situ stress state of 10 MPa (green line); (ii) axial loading up to the peak stress (36.77 MPa) and stress drop (30.36 MPa) at a constant axial displacement rate of 1 mm/hour (plain red line); (iii) axial loading at a constant displacement rate of 10 mm/hour during which the axial stress variation is non monotonic (sudden increase to 31.09 MPa, slower decrease to 29.92 MPa, then even slower increase to reach a plateau at 32.82 MPa. The failed specimen obtained after the experiment is pictured on the right hand side.

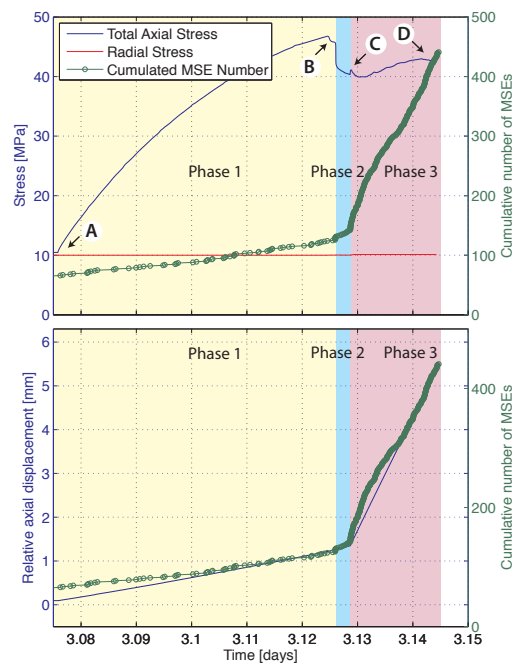


Figure 4: Evolution with time of the total axial and radial stresses, axial displacement and cumulative number of micro-seismic events during Phases 1 (A to B in yellow), 2 (B to C in blue) and 3 (C to D in pink) of the experiment. Over all, the cumulative number of events is linearly related to the axial displacement rate, except temporarily after the increase in the imposed displacement rate from 1 to 10 mm/hour and until the axial stress reaches a plateau.

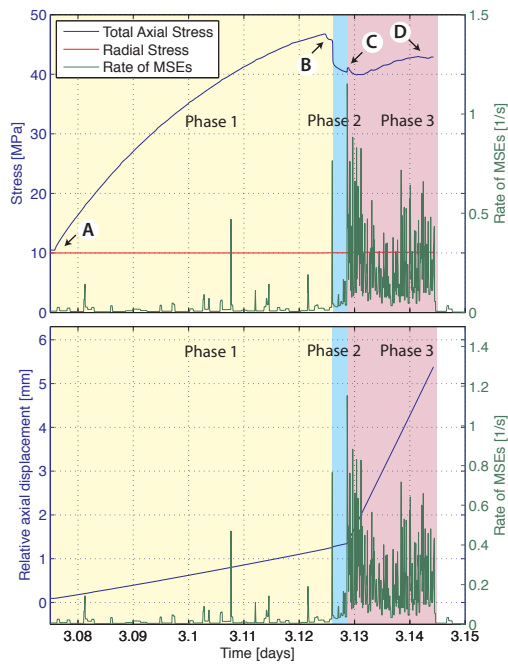


Figure 5: Evolution with time of the total axial and radial stresses, axial displacement and rate of micro-seismic activity during Phase 1 (A to B in yellow), 2 (B to C in blue) and 3 (C to D in pink) of the experiment. The rate of micro-seismic activity (amplitude of the green curve) is strongly correlated with the imposed displacement rate (slope of the blue curve in the lower graph) and the evolution of the axial stress (amplitude of the blue curve in the upper graph).

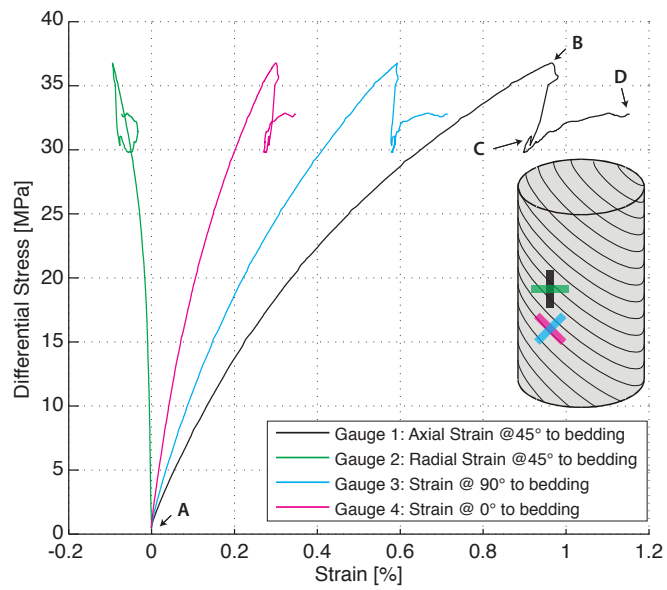


Figure 6: Stress-strain data during Phase 1 (A to B), 2 (B to C) and 3 (C to D) of the experiment. The orientation of the strain gauges with respect to the shale bedding and the specimen's axis are also shown. The strain recorded by the gauges illustrates the mechanical anisotropy of the shale.

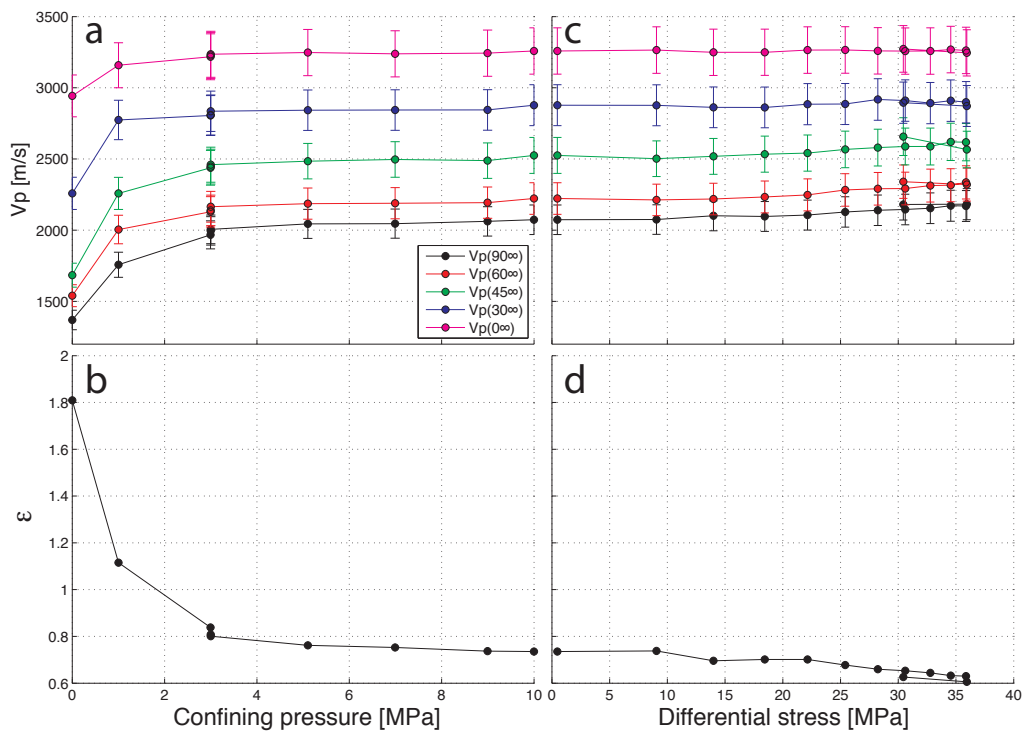


Figure 7: Evolution of P-wave group (ray) velocity and anisotropy (Thomsen's ϵ parameter) with confining pressure and deviatoric loading. P-wave velocity data are indicated with a 10% error bar (+/- 5%). The magnitude of the P-wave velocity as a function of the propagation direction with respect to the bedding illustrates the elastic anisotropy of the shale. This anisotropy decreases significantly with increasing confining pressure, and is virtually not sensitive to the axial stress, at least until the strain localises in a shear fault and the specimen fails. The non-linear variation of the P-wave velocity with confining pressure up to about 4 MPa suggests the existence of damage in the shale specimen at

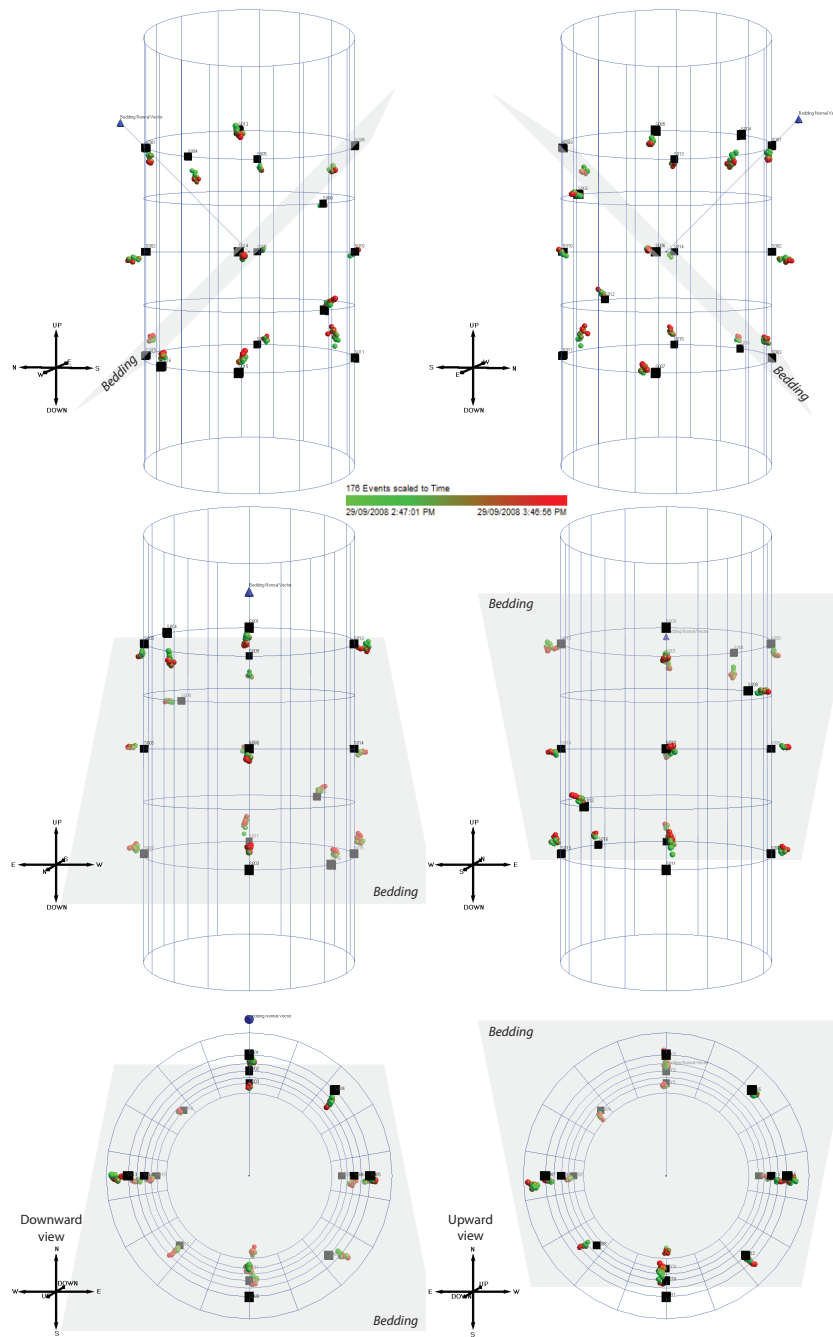


Figure 8: Spatial and temporal location of the ultrasonic sources shot during the velocity surveys. The squares represent the nominal position of the centre of the ultrasonic sensors; the spheres represent the location of the sources obtained by inversion using the selected velocity model.

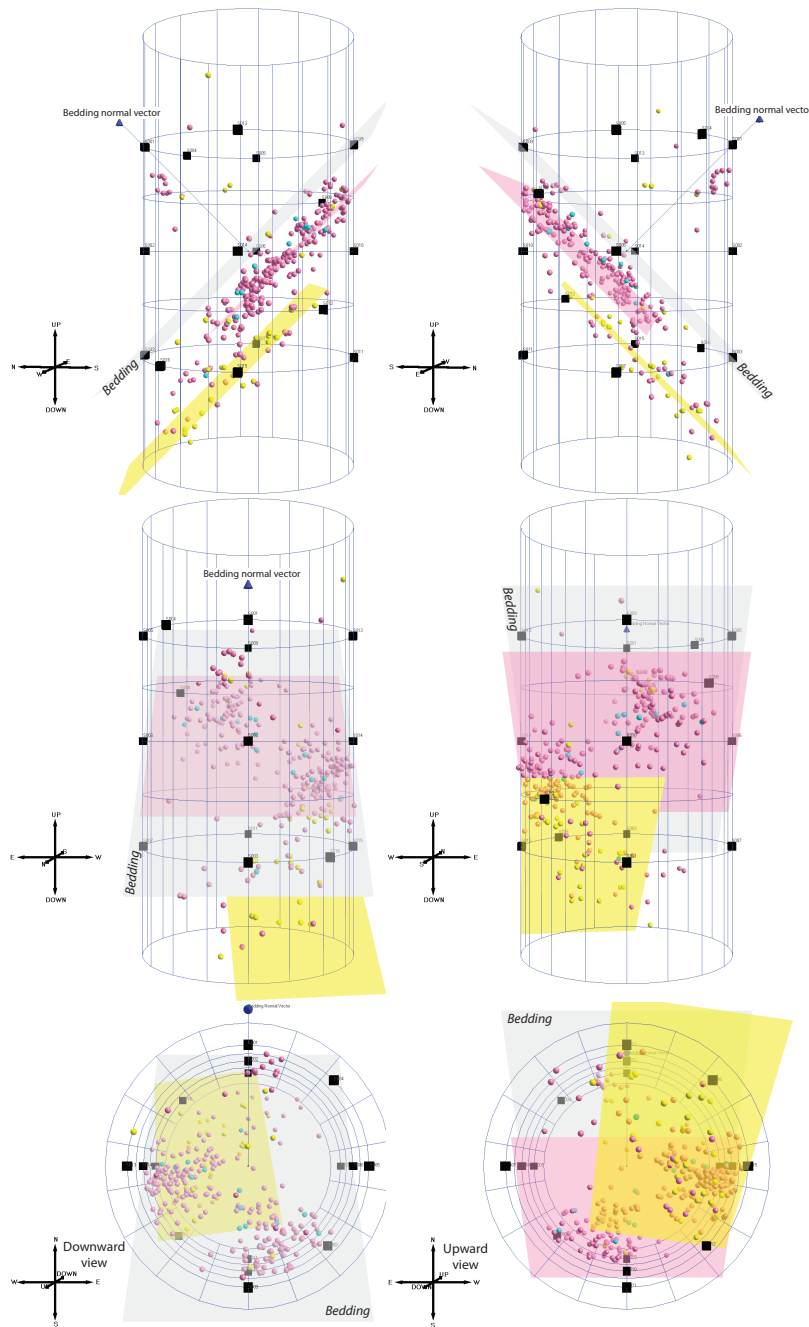


Figure 9: Spatial and temporal location of the micro-seismic events recorded during the three phases of the deviatoric loading: in yellow for Phase 1; in blue for Phase 2; and in pink for Phase 3. The micro-seismic activity suggests the existence of two overlapping shear fault planes. Part of the micro-seismic activity locates in the overlap volume between these two planes. A feature similar to relay ramps observed in large scale structural geology.

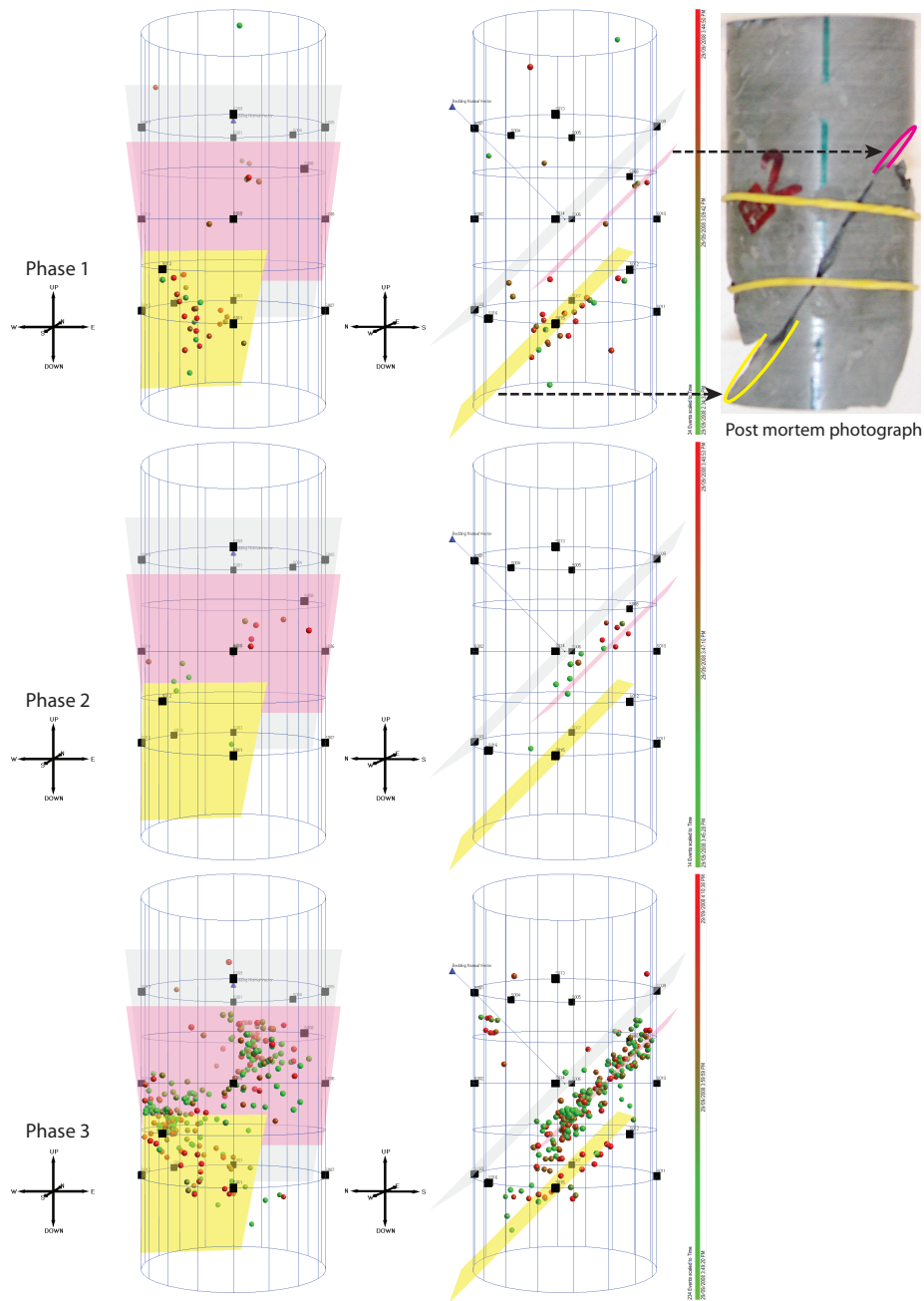


Figure 10: Spatial and temporal location of the recorded MSEs separated into the three phases of the experiment. For each phase, the color of each event is scaled to its time of occurrence, i.e., first events of the phase in green and last events in red. These results suggest that the lower shear fault (yellow plane) is most active (accommodates most of the imposed axial displacement) at the early stages after strain localisation (Phase 1). During Phase 2, a transition of the micro-seismic activity is observed from the lower shear fault toward the upper shear fault (pink plane). During Phase 3 most of the imposed axial displacement is accommodated by the upper shear fault although few events are still

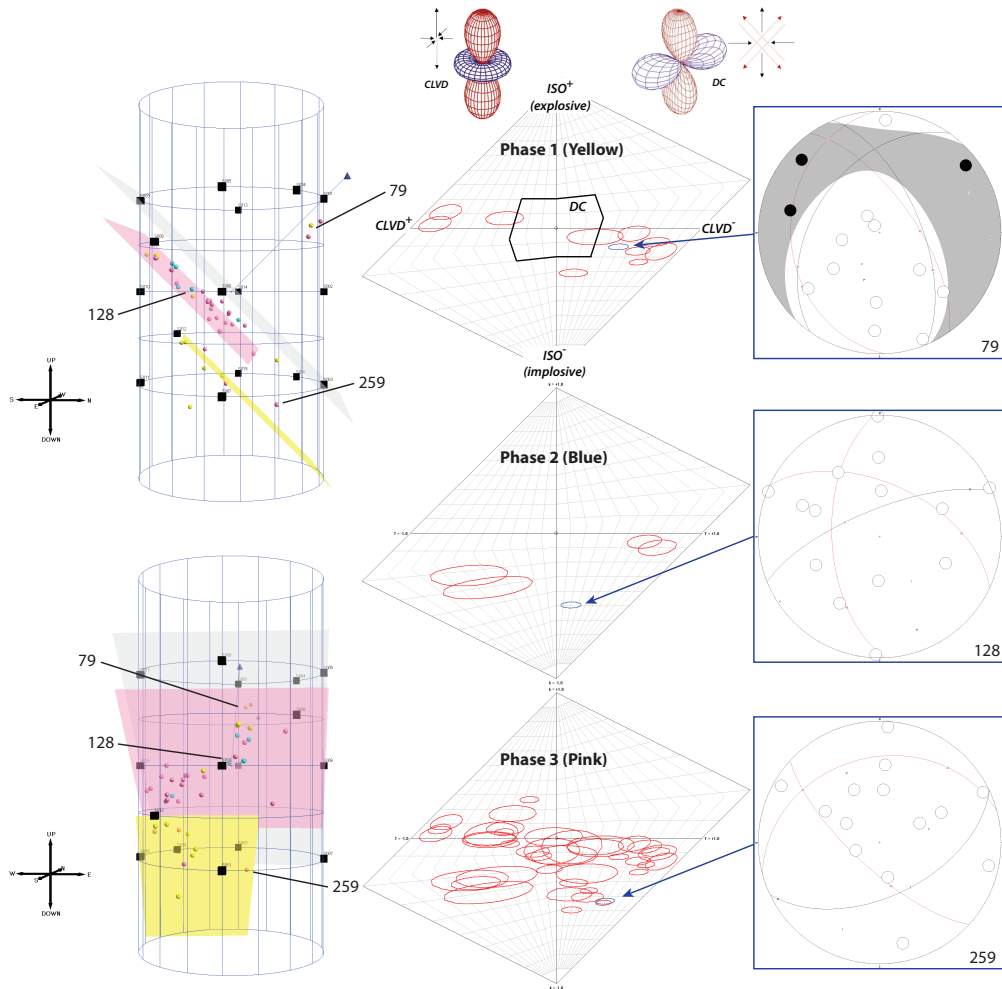


Figure 11: Spatial location, T-k decomposition in Hudson's diagram [23], and moment tensor solution of the MSE with largest magnitude in each of the three phases of the experiment: MSE #79 in Phase 1, MSE #128 in Phase 2 and MSE #259 in Phase 3.

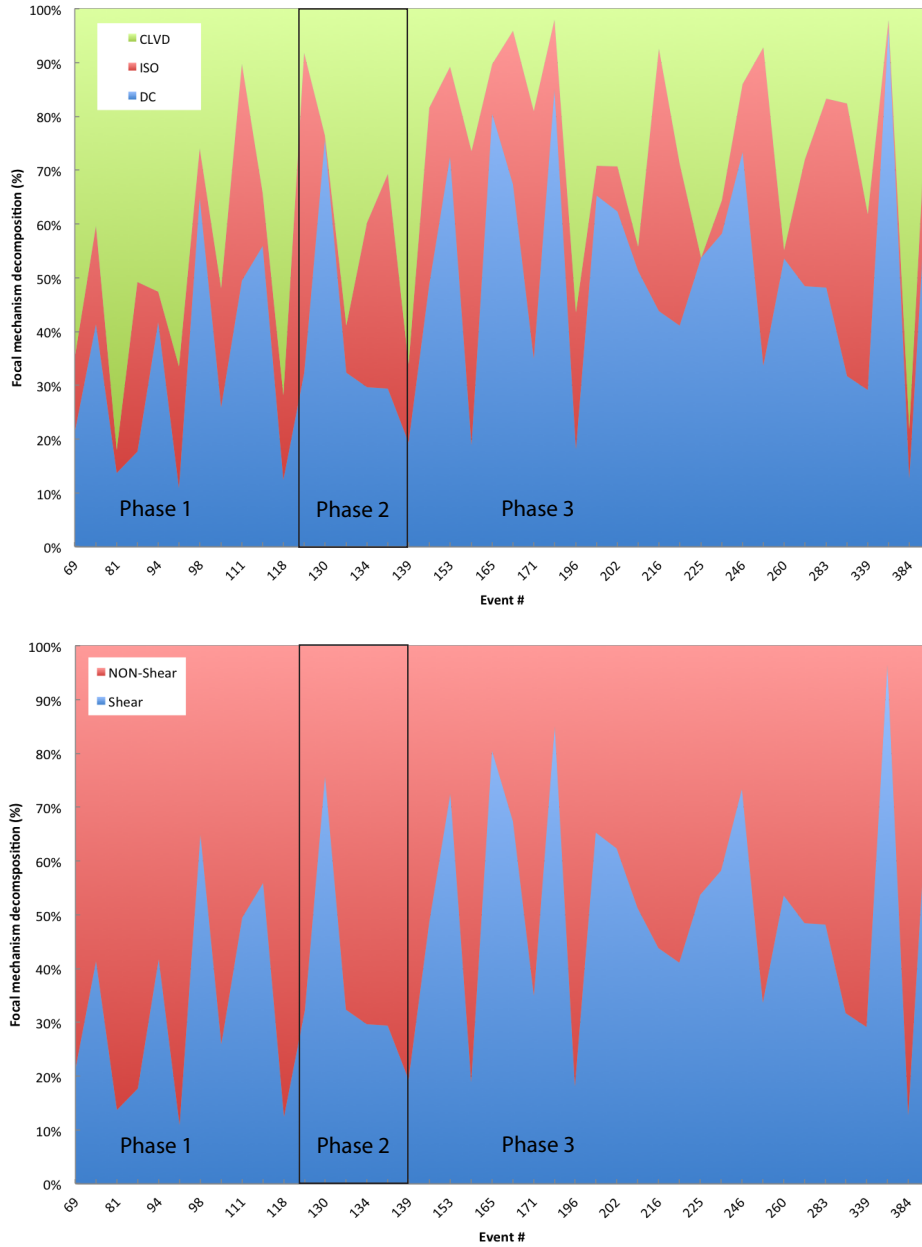


Figure 12: Results of the moment tensor decomposition of the selected high quality MSEs. The top plot shows the detailed decomposition into DC, CLVD and ISO MSEs; the lower plot shows the simpler decomposition into shear and non-shear MSEs (see main text for details).

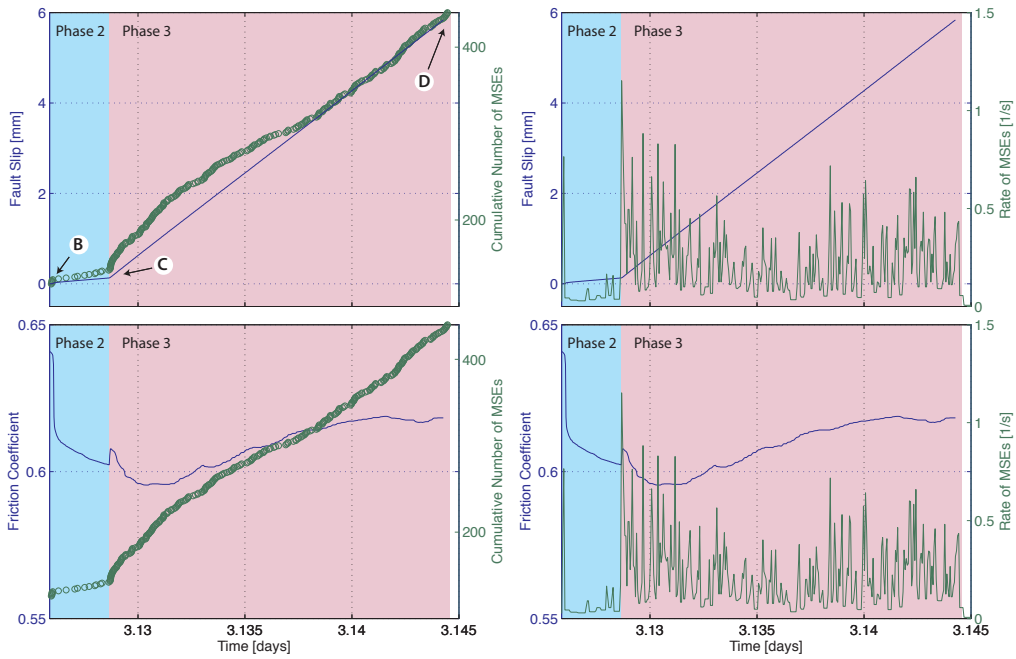


Figure 13: Fault frictional behaviour and MS activity during Phases 2 and 3. The fault slip is calculated from the measured post-failure axial displacement and the orientation of the fault plane determined post mortem to be approximately at 45° to the specimen's axis.